

OBSERVATIONS AND MAGNETIC FIELD MODELING OF THE FLARE/CORONAL MASS EJECTION EVENT ON 2010 APRIL 8

YINGNA SU¹, VINCENT SURGES^{1,2}, ADRIAAN VAN BALLEGOOIJEN¹, EDWARD DELUCA¹, AND LEON GOLUB¹

¹Harvard-Smithsonian Center for Astrophysics, Cambridge, MA 02138, USA; ynsu@head.cfa.harvard.edu

²The College of St. Scholastica, Duluth, MN 55811, USA

Received 2010 December 29; accepted 2011 March 30; published 2011 May 24

ABSTRACT

We present a study of the flare/coronal mass ejection event that occurred in Active Region 11060 on 2010 April 8. This event also involves a filament eruption, EIT wave, and coronal dimming. Prior to the flare onset and filament eruption, both *SDO/AIA* and *STEREO/EUVI* observe a nearly horizontal filament ejection along the internal polarity inversion line, where flux cancellations frequently occur as observed by *SDO/HMI*. Using the flux-rope insertion method developed by van Ballegoijen, we construct a grid of magnetic field models using two magneto-frictional relaxation methods. We find that the poloidal flux is significantly reduced during the relaxation process, though one relaxation method preserves the poloidal flux better than the other. The best-fit pre-flare NLFFF model is constrained by matching the coronal loops observed by *SDO/AIA* and *Hinode/XRT*. We find that the axial flux in this model is very close to the threshold of instability. For the model that becomes unstable due to an increase of the axial flux, the reconnected field lines below the X-point closely match the observed highly sheared flare loops at the event onset. The footpoints of the erupting flux rope are located around the coronal dimming regions. Both observational and modeling results support the premise that this event may be initiated by catastrophic loss of equilibrium caused by an increase of the axial flux in the flux rope, which is driven by flux cancellations.

Key words: Sun: coronal mass ejections (CMEs) – Sun: filaments, prominences – Sun: flares – Sun: magnetic topology – Sun: UV radiation – Sun: X-rays, gamma rays

Online-only material: color figures, animations

1. INTRODUCTION

The most commonly seen chromospheric flare morphology is the two-ribbon flare, according to Tang (1985). The two flare ribbons usually appear in pairs and separate with time. Accompanying the flare ribbons is a system of flare loops which initially appears at low altitude and then moves upward into the corona in consort with the ribbon's separation (Moore et al. 1980). The ribbon separation and flare loop expansion are interpreted as the result of progressive reconnection in the corona above the ribbons, in which new magnetic field lines reconnect at higher and higher altitudes, according to the classical two-dimensional “CSHKP” model for two-ribbon flares (Svestka & Cliver 1992). Filament eruptions and coronal mass ejections (CMEs) are often associated with two-ribbon flares. Extreme Ultraviolet (EUV) observations of the lower corona reveal two (often global-scale) dynamic phenomena closely linked to the origins of CMEs: “coronal waves” and “dimmings” (Zhukov & Auchère 2004). Arcade formation and coronal dimmings are identified as the soft X-ray counterpart of CMEs (Kosugi & Acton 2002). It has been suggested that the dimmings mark the position of flux-rope footpoints (Webb et al. 2000). Upon eruption of the flux rope, the magnetic loops rooted in the dimming regions “open” to the solar wind. The regions become dark as plasma expands or escapes along the open field lines (Thompson et al. 2000).

Solar flares, filament eruptions, and CMEs are different manifestations of a single physical process thought to be powered by the release of magnetic free energy stored in the corona prior to the event. Storage of free energy requires a non-potential magnetic field, and is therefore associated with shear and/or twist in the coronal field (Priest & Forbes 2002).

Twisted or sheared magnetic fields are often visible in the solar corona before solar eruptions (Rust & Kumar 1996; Canfield et al. 1999; Moore et al. 2001; Su et al. 2007a, 2007b), but it is unclear how the eruption initiates. To determine what triggers such eruptions and how the energy is released, it is important to understand the three-dimensional (3D) structure of the coronal magnetic field prior to and during the eruption.

There are two groups of competing models for the pre-eruption magnetic configuration. One group of models assume that a twisted flux rope is present in the region above the polarity inversion line (PIL) on the photosphere (Forbes & Isenberg 1991; Gibson & Low 1998; Krall et al. 2000; Wu et al. 1997; Roussev et al. 2003). The other group of models begin with an untwisted, but highly sheared magnetic field (Mikic & Linker 1994; Antiochos et al. 1999; Amari et al. 2003a; Manchester 2003). In both cases, the flux rope or the sheared arcade is held down by the tension of the overlying coronal arcade. According to the latter models, a twisted flux rope does not exist prior to eruption, but is formed during the eruption as a result of reconnection between the two sides of the sheared arcade. Therefore, in both types of models a twisted flux rope is present in the ejecta. The existence of such flux ropes is confirmed by in situ observations of magnetic fields in interplanetary magnetic clouds (Burlaga 1991). However, the question of when and how such flux ropes are formed remains.

Several mechanisms have been proposed to trigger the eruption. According to the magnetic breakout model (Antiochos et al. 1999), the CME onset is triggered by reconnection occurring at the top of a sheared arcade, which then allows the flux to escape. Other possibilities include shearing and/or converging motions in the photosphere (Forbes et al. 1994; Mikic & Linker 1994; Antiochos et al. 1994), magnetic flux

emergence (Chen & Shibata 2000), and flux cancellation (van Ballegoijen & Martens 1989; Linker et al. 2001). Recently, kink instability has received more attention (Williams et al. 2005; Rust & LaBonte 2005; Fan & Gibson 2007; Savcheva & van Ballegoijen 2009). Eruptions may be triggered by “catastrophic loss of equilibrium” in response to slow evolution of the magnetic fields in the photosphere (Forbes 1990; Lin & Forbes 2000). Finally, the drainage of plasma from a prominence may play a role in destabilizing flux ropes on the quiet Sun (Low et al. 2003). At present, it is often unclear which of these mechanisms or combinations is responsible for any particular event.

Three-dimensional MHD CME models have been developed by many authors (e.g., Linker & Mikic 1995; Amari et al. 2003a, 2003b; Manchester et al. 2004; Fan & Gibson 2007; Lynch et al. 2008). These models can obtain a full picture of the 3D evolution of the coronal magnetic field during the eruption. They are useful for demonstrating both CME initiation and propagation in a single calculation. However, all of these models use idealized magnetic configurations, which only mimic the real magnetic configurations, along with idealized footpoint motions. Taking into account a more realistic coronal environment might affect the modeling result significantly. Several 3D MHD simulations have been carried out for a few relatively “simple” events having extensive observational data (e.g., Manchester et al. 2008; Cohen et al. 2009, 2010, and references therein). However, most of these simulations have very low spatial resolution, and they focus on the propagation of the CME. To our knowledge, very few attempts (Titov et al. 2010; Bisi et al. 2010) have been made to produce 3D MHD simulations of a real flare/CME event and to make detailed comparisons with the source region and flare observations in the lower corona.

In the last few years, we have developed various tools for modeling non-potential magnetic fields in the solar corona, called the Coronal Modeling System (CMS; van Ballegoijen 2004). The CMS software has been used successfully in studies of a filament (van Ballegoijen 2004), active regions (Bobra et al. 2008; Su et al. 2009a, 2009b), and a coronal X-ray sigmoid (Savcheva & van Ballegoijen 2009). In these studies, nonlinear force-free field (NLFFF) models were constructed not by extrapolating an observed photospheric vector field into the corona (e.g., Canou & Amari 2010; Cheng et al. 2010; Guo et al. 2010; Fuhrmann et al. 2011), but rather by inserting a magnetic flux rope into a potential-field model of the active region and then applying magneto-frictional relaxation (e.g., Yang et al. 1986; van Ballegoijen et al. 2000). This flux-rope insertion method is quite flexible and provides information about the stability of the resulting fields. The models are constrained by observed non-potential structures such as H α filaments and sheared or twisted coronal loops. The models use variable grid spacing to achieve high spatial resolution in the lower corona (e.g., 0.002 R_{\odot}) while covering a large coronal volume in and around the target region. Our previous work demonstrated the capability of the CMS software for modeling the non-potential field prior to the eruption. In the present work, we create two magnetic models for Active Region 11060, which produced a flare/CME event on 2010 April 8: (1) a best-fit NLFFF model of the region prior to the eruption and (2) an unstable model that represents the early stage of the eruption. We will then compare our models with observations prior to and during the eruption.

2. INSTRUMENTS

The event under study is well observed by the Atmospheric Imaging Assembly (AIA; Lemen et al. 2011) aboard the

Table 1
AIA Wavelength Bands

Channel Name	Primary Ion(s)	Char. T (MK)
White light	Continuum	0.005
1700 Å	Continuum	0.005
304 Å	He II	0.05
1600 Å	C IV + cont.	0.1
171 Å	Fe IX	0.6
193 Å	Fe XII, XXIV	1.6, 20
211 Å	Fe XIV	2
335 Å	Fe XVI	2.5
94 Å	Fe XVIII	6.3
131 Å	Fe VIII, XXI	0.4, 10

Solar Dynamics Observatory (SDO), as well as the *STEREO/EUVI* (Wuelser et al. 2004). AIA consists of seven EUV and three Ultraviolet (UV) visible channels, which allows for an unprecedented look at the thermal structure in solar flares (Reeves & Golub 2011). The primary ions and emission temperature for each passband are listed in Table 1. AIA takes images that span at least 1.3 solar diameters ($2458'' \times 2458''$) in multiple wavelengths nearly simultaneously. The AIA pixel size is $0''.6$, and the resolution is about $1''$ depending on wavelength. The nominal cadence for AIA is 12 s, but at the time of the present observations *SDO* was still in its commissioning phase, and the cadence of the observations is 20 s. The associated CME event was observed with the coronagraphs on *STEREO* (Howard et al. 2008) and the *Solar and Heliospheric Observatory/Large Angle and Spectrometric Coronagraph Experiment (SOHO/LASCO)*; Brueckner et al. 1995). Synoptic observations by the X-Ray Telescope (XRT; Golub et al. 2007; Kano et al. 2008) aboard *Hinode* (Kosugi et al. 2007) and H α observations by the Kanzelhöhe Solar Observatory (KSO) are also included in the study. The X-ray light curves of the flare are provided by *GOES*. The photospheric magnetic field information is provided by the Helioseismic and Magnetic Imager (HMI; Schou et al. 2011) aboard *SDO*. HMI is an instrument designed to study oscillations and the magnetic field at the solar surface, or photosphere. HMI observes the full solar disk at 6173 Å with $0''.5$ pixels.

3. OBSERVATIONS

3.1. Structure of the Flaring Region

A *GOES* B3.7 two-ribbon flare occurred in NOAA Active Region 11060 (N25E16) around 02:30 UT on 2010 April 8. Multi-wavelength observations of the flaring active region prior to the flare are shown in Figure 1. The line-of-sight (LOS) magnetogram taken by *SDO/HMI* (Figure 1(a)) shows that this region is a dispersed bipolar active region without significant sunspots. The white and black spots refer to the positive and negative polarities, respectively. The thick white line between the two polarities refers to the smoothed internal PIL. Only a short filament along the northern part of the internal PIL can be identified on the H α image taken by KSO on April 7 (white arrow in Figure 1(b)). The pixel size of the H α image is around $1''$. Figure 1(c) shows the AIA image at 304 Å, which contains two filaments. The thin dark filament along the internal PIL is marked with a black arrow, and the white arrow marks the filament surrounding the active region. The internal filament is also visible in the 171 Å and 335 Å images (Figures 1(d) and (e)). More loops in the core of the active region are visible at 335 Å than at 171 Å. Figure 1(e) shows that this region mainly

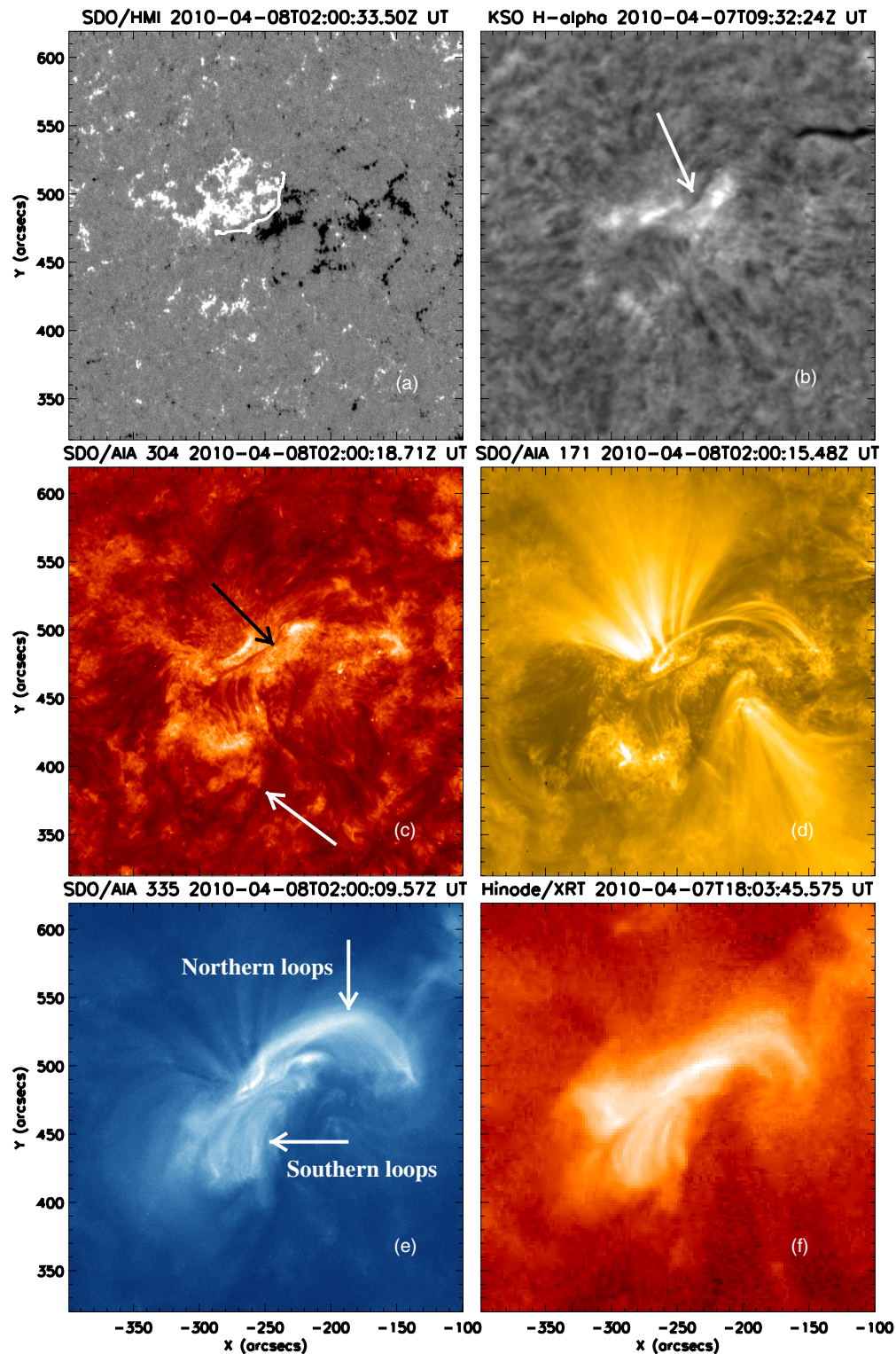


Figure 1. Multi-wavelength observations of AR 11060 prior to the B3.7 flare on 2010 April 8. (a) LOS magnetogram taken by HMI aboard *SDO*. The thick white line refers to the smoothed PIL. (b) $H\alpha$ image taken by KSO. (c)–(e) EUV images at 304 Å, 171 Å, and 335 Å observed by *SDO/AIA*. (f) X-ray image observed by *Hinode/XRT* using the Ti-poly filter. In panel (c), the black arrow refers to the filament at the core of the active region, and the filament surrounding the active region is marked with a white arrow. The field of view of each image is $300'' \times 300''$.

(A color version of this figure is available in the online journal.)

contains two sets of bright loops: loops in the northern part and loops in the southern part. The only XRT observation of this region (Figure 1(f)) before the flare is the synoptic image taken 7 hr earlier than the AIA image shown in Figure 1(e). The pixel size of the XRT image in Figure 1(f) is around $2''$. The southern

loops at 335 Å look similar to that in the XRT images, but the northern loops show different structure in these two images (i.e., Figures 1(e) and (f)). This may be due to the evolution of the active region with time, since there is a 7 hr time difference between the two images.

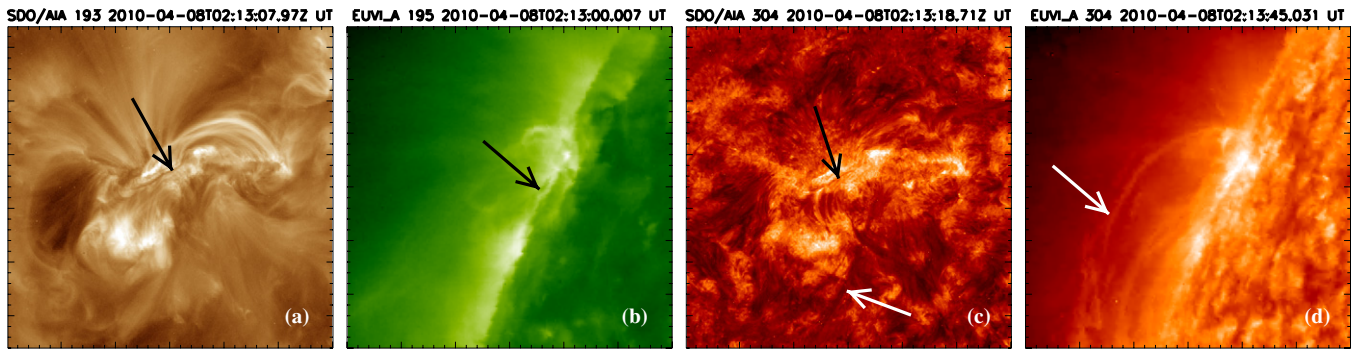


Figure 2. *SDO/AIA* and *STEREO/EUVI* observations of AR 11060 at 02:13 UT on 2010 April 8 at different wavelengths. The filament at the core of the active region is marked with the black arrow, and the white arrow refers to the filament surrounding the active region. The field of view of each image is $300'' \times 300''$. The evolution of the event is also available as an animation in the online version of the journal. The online animation has a larger field of view ($547'' \times 547''$.)

(An animation and a color version of this figure are available in the online journal.)

3.2. Time Evolution of the Event

The flare under study appears to be associated with a CME ($v = 174 \text{ km s}^{-1}$) started around 03:30 UT as observed by *SOHO/LASCO*. The CME first appears in COR 2 aboard *STEREO Ahead* at 03:54 UT, and the median CME speed is around 510 km s^{-1} . The CME information is provided by the CACTUS CME Catalog³ (Robbrecht et al. 2009). A global EUV disturbance (the so-called EIT wave) is also involved in this event. A detailed study on the EUV wave involved in this event (Liu et al. 2010) suggests that the disturbance exhibits two components: one diffuse pulse on which are superimposed multiple sharp fronts that have fast and slow components. This event is well observed by *SDO/AIA* with 20 s cadence at multiple UV and EUV passbands. The *SDO* data used in this study are the level 0 data. *STEREO Ahead/EUVI* caught this event at the east limb. A snapshot of AR 11060 prior to the event is shown in Figure 2, and video 1 (online animation) shows a movie of this event observed by *AIA* and *EUVI*. The black and white arrows in Figure 2 refer to the internal filament and the filament surrounding the active region, respectively. Figure 3 shows observations from three representative *AIA* channels at different stages of the event. The top, middle, and bottom rows of Figure 3 show *AIA* images from hotter to cooler channels, respectively, i.e., 94 Å, 193 Å, and 304 Å.

Around 02:10 UT, material from the internal filament started to eject nearly horizontally along the PIL from the north to the south. About 18 minutes later, the internal filament began to lift off which is followed by the first flare brightenings and the eruption of the surrounding filament. The eruption of the internal filament is best seen at 195 Å by *STEREO Ahead*. No clear evidence of the eruption of the internal filament can be identified from the *AIA* observations due to the projection effect. The first flare brightenings are shown in the left column of Figure 3. These brightenings are located on the two sides of the internal filament (marked as black dashed lines), and appear to be the conjugate footpoints of newly reconnected flare loops. Figure 3(a) shows that these flare footpoints are highly sheared, i.e., the angle between the line connecting the two footpoints and the line perpendicular to the PIL is large. The black dashed line in Figure 3 is a sketch of the PIL based on the smoothed internal PIL as shown in Figure 1(a). The second column displays images from 02:40 UT, about 10 minutes after the flare onset. At this stage, the flare ribbons are visible at 193 Å and 304 Å, and

remain close to each other, while the flare loops are seen at 94 Å. Figure 3(b) shows that the flare loops are highly sheared at this stage, which is consistent with Figure 3(a). As the flare continues to erupt, the ribbons become further separated from one another, and post-flare loops begin to appear in 193 Å (see the third column). At about 03:15 UT, the first signs of coronal dimmings appear in 193 Å. The dimming regions started to recover around 04:40 UT, but are still visible at 05:59 UT as shown in Figure 3(h). After the eruption is well underway, nearly potential post-flare loops are visible in all channels (last column), i.e., the loops are nearly perpendicular to the PIL.

The *GOES* and *AIA* light curves of the event are shown in Figure 4. The first row displays temporal evolution of the total flux observed at two soft X-ray channels by *GOES*. The other eight rows of Figure 4, from top to bottom, show the light curves of the event from hotter to cooler *AIA* channels, respectively. The yellow (gray) lines refer to the average data number (DN) measured within a region of $300'' \times 300''$ as shown in Figure 1. The black light curves refer to the mean DN measured within a smaller region ($156'' \times 92''$) enclosed in the black box as shown in Figure 3(h). The black *GOES* light curve shows that this flare starts around 02:30 UT, peaks at 03:35 UT. The light curves for the three hotter *AIA* channels (131 Å, 94 Å, 335 Å) look similar to the black *GOES* light curve. Among all of the *AIA* channels, the light curve at 94 Å is the one that looks closest to the black *GOES* light curve. The light curves for the two cooler *AIA* channels (1600 Å and 304 Å) share similar characteristics, especially the flare peak time is earlier than the other channels. Note that the spikes in the 1600 Å channel appear to be dominated by the 5 minute oscillations. The black and yellow (gray) light curves are consistent with each other for most of the *AIA* channels except the three middle channels (211 Å, 193 Å, 171 Å). The yellow (gray) light curves for these channels display a clear decrease starting around 03:00 UT, then the emission remains lower than the pre-flare phase until 05:00 UT. This decrease is corresponding to the coronal dimmings as seen in these channels. The coronal dimming is excluded for the black light curves. Unlike the *GOES* light curve, the strongest emission in the black light curves for the three *AIA* middle channels (211 Å, 193 Å, 171 Å) occurs after 05:00 UT. In fact, the emission increase after 05:00 UT is also visible in the two hotter channels (131 Å and 335 Å). This emission increase corresponds to the brightening of post-flare loops.

Figure 5 shows the LOS photospheric magnetograms taken by *SDO/HMI* at three different times prior to and after the flare. The cadence of the *HMI* observations is 45 s. An online

³ <http://sidc.oma.be/cactus/>

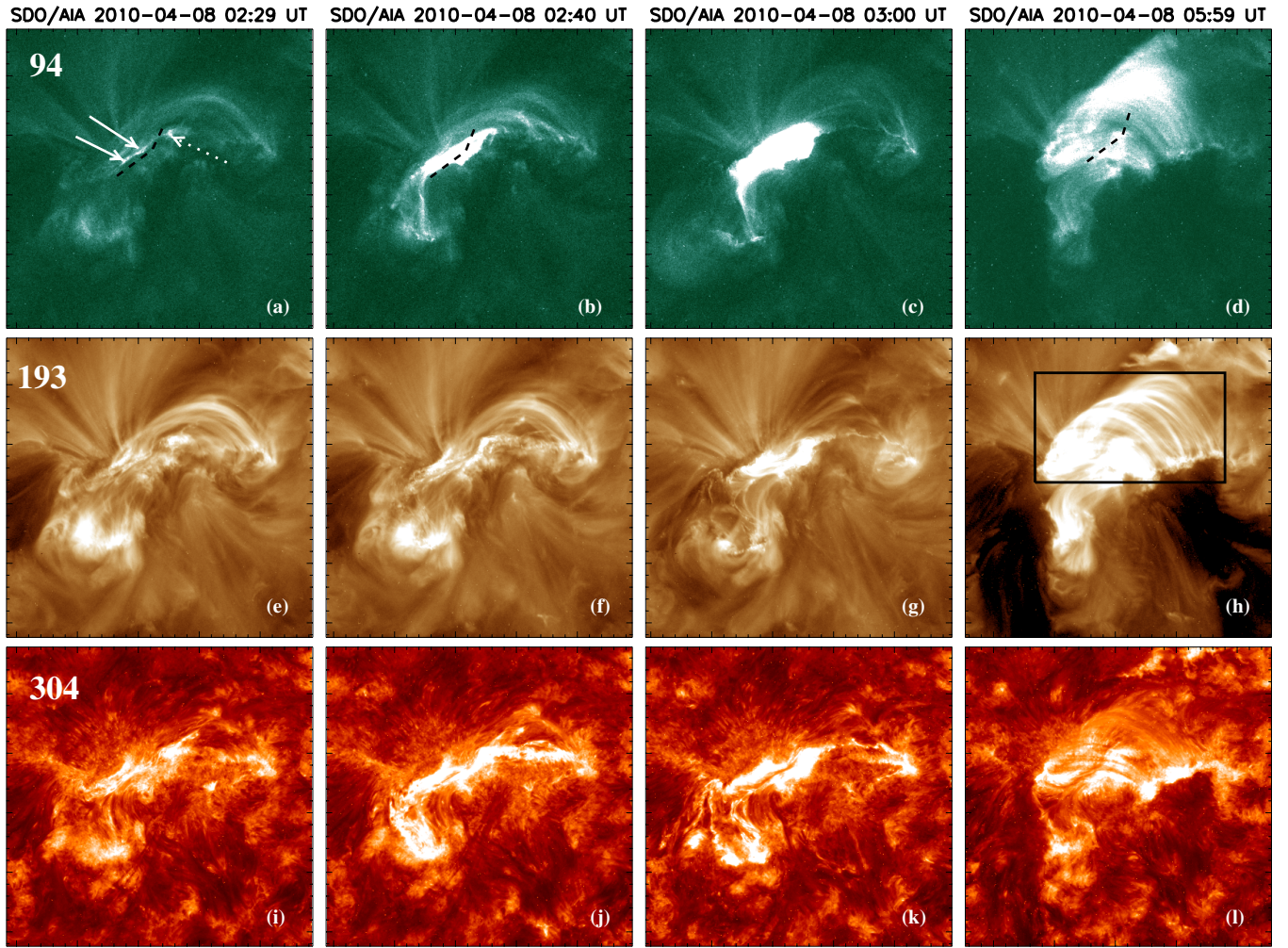


Figure 3. *SDO/AIA* observations of the flare/CME event on 2010 April 8 at three different wavelengths. The top row shows the event at 94 Å. The second row depicts the flare at 193 Å, while images at 304 Å are displayed in the bottom row. The black dashed lines in the top row represent the locus of the H α filament observed around 9:00 UT by KSO. The black box in panel (h) enclosed the main flaring region. The field of view of each image is 251'' \times 251''.

(A color version of this figure is available in the online journal.)

animation (video 2) shows the evolution of the magnetic fields from 21:00 UT on April 7 to 06:00 UT on April 8. Clear evidence of flux cancellations near the PIL is identified both prior to and during the eruption. For example, flux cancellations occurred in the region enclosed in the white box between 21:00 UT and 24:00 UT (Figures 5(a) and (b)) on April 7. Flux cancellations started in the black-box region right before and during the flare on April 8 as shown in Figures 5(b) and (c).

4. MAGNETIC FIELD MODELING

4.1. Flux-rope Insertion Method

Our magnetic field models are created using the flux-rope insertion method developed by van Ballegoijen (2004). This method only requires LOS photospheric magnetograms, i.e., the radial component of the magnetic field in the photosphere. This method involves inserting a magnetic flux rope along a selected filament path into a 3D potential-field model. First a modified potential-field model of AR 11060 is constructed based on the LOS magnetogram observed by *SDO/HMI* at 02:00 UT on 2010 April 8, which is shown as red and green contours in Figure 6. The total magnetic flux of this active region (as measured in a field of view that is shown in Figure 5) is about 3.7×10^{21} Mx. Figure 6 shows that the internal filament has sinis-

tral orientation with respect to the surrounding photospheric fields, and therefore is an exception to the hemispheric rule (Martin 1998). The potential field reproduces the coronal arcade that overlies the flux rope and prevents it from erupting into the heliosphere. The next step is to specify the parameters of the flux rope, including its path on the solar surface and its axial and poloidal fluxes. The blue curve terminating with two circles in Figure 6 represents the path which is selected based on the observed location of the H α filament. The length of the blue curve is about 97 Mm. We then modify the potential field to create a cavity in the region above the selected path. In essence, the field lines immediately above the path are pushed upward, creating a region with $B \approx 0$. A flux rope with sinistral orientation is then inserted into this cavity. The axial flux (Φ_{axi}) of the flux rope is represented by a thin tube that runs horizontally along the length of the selected path (at a small height above the photosphere). At the two ends of the path, the tube is anchored in the photosphere via two vertical sections. The poloidal flux (F_{pol}) is inserted as a set of closed field lines that wrap around this tube. We define $F_{\text{pol}} > 0$ for a flux rope with right-handed twist.

The above field configuration is not in force-free equilibrium. So our next step is to use magneto-frictional relaxation to drive the field toward a force-free state. This method is an iterative

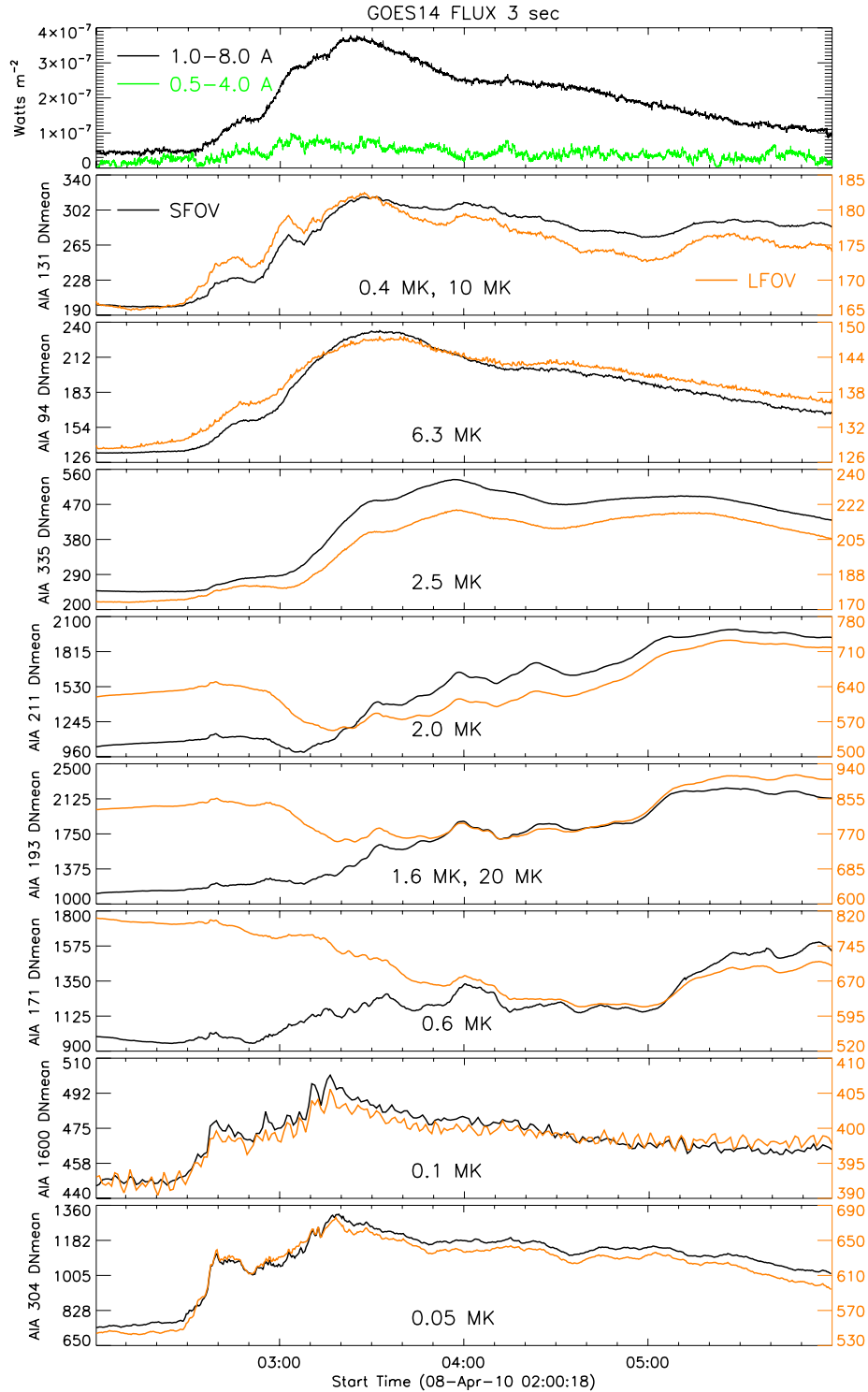


Figure 4. *GOES* (top row) and *SDO/AIA* (other rows) light curves of the flare/CME event on 2010 April 8 at different wavelengths. The yellow (gray) *AIA* light curves refer to the average DN in a region with a $300'' \times 300''$ field of view as shown in Figure 1. The black *AIA* light curves represent the average DN within a smaller region $156'' \times 92''$, as shown in the black box in Figure 3(h).

(A color version of this figure is available in the online journal.)

relaxation method (van Ballegooijen et al. 2000) specifically designed for use with vector potentials. Specifically, we solve the following equation:

$$\frac{\partial \mathbf{A}}{\partial t} = \eta_0 \mathbf{v} \times \mathbf{B} - \eta_2 \nabla \times \mathbf{B} + \frac{\mathbf{B}}{B^2} \nabla \cdot (\eta_4 B^2 \nabla \alpha) + \nabla (\eta_d \nabla \cdot \mathbf{A}), \quad (1)$$

where \mathbf{v} is the plasma velocity, η_0 , η_2 , η_4 , and η_d are constants in space, and $\alpha \equiv \mathbf{j} \cdot \mathbf{B} / B^2$, where $\mathbf{j} = \nabla \times \mathbf{B}$. The velocity is given by

$$\mathbf{v} = (f \mathbf{j} - v_1 \hat{\mathbf{r}} \times \mathbf{B}) \times \mathbf{B} / B^2, \quad (2)$$

where f is the coefficient of magnetofriction and v_1 describes the effects of buoyancy and pressure gradients in the photosphere (Bobra et al. 2008). Magnetofriction has the effect of expanding

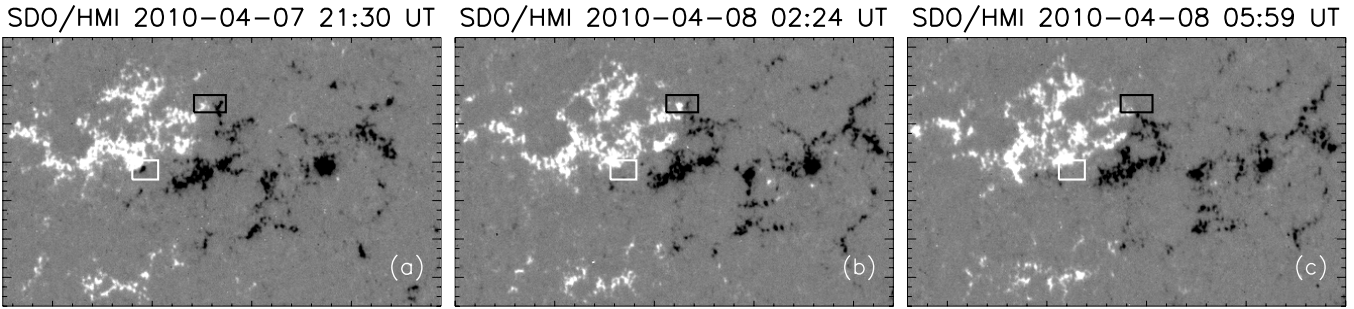


Figure 5. Line-of-sight photospheric magnetograms taken by *SDO/HMI* prior to and after the flare. The black and white boxes mark the regions with clear flux cancellations.

(An animation of this figure is available in the online journal.)

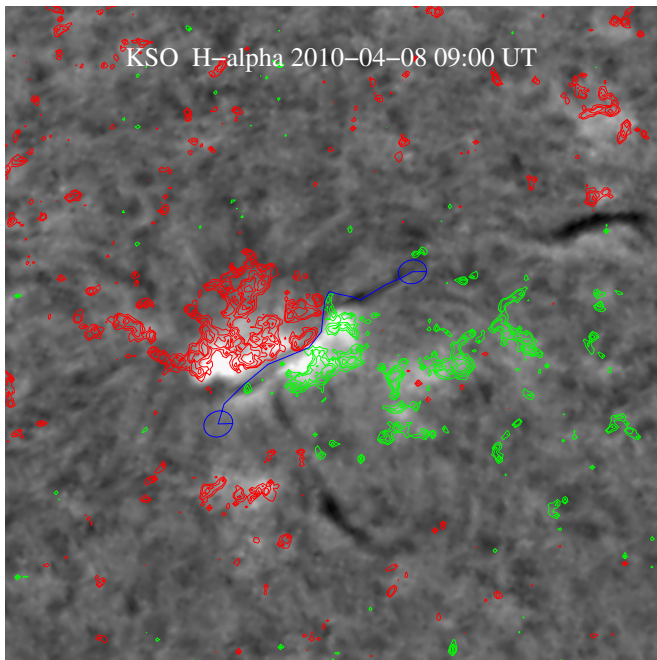


Figure 6. $H\alpha$ image observed at 9:00 UT on April 8 by KSO. The blue line ending with two circles refers to the selected filament path for inserting the flux rope. The red and green contours represent the positive and negative magnetic fields taken by *SDO/HMI* at 02:00 UT on April 8. The field of view of this figure is $0.32 R_{\odot}$.

the flux rope until its magnetic pressure balances the magnetic tension applied by the surrounding potential arcade. Significant magnetic reconnection between the inserted flux rope and the ambient flux may occur during the relaxation process. Therefore, the end points of the flux rope in the relaxed model may be different from that in the original model.

Our previous studies (Bobra et al. 2008; Su et al. 2009a, 2009b; Savcheva & van Ballegoijen 2009) were based on CMS Version 1.0, in which the computational domain is a wedge-shaped volume in the corona surrounding an observed active region and a filament. The domain extended from the photosphere to a “source surface” at a radial distance of about $2 R_{\odot}$ from the Sun center. We used periodic boundary conditions in longitude and closed boundaries in latitude. In the current study, we use CMS Version 2.0, which includes a description of the global corona to improve the boundary conditions. The object of interest (e.g., an active region or a filament) is modeled with high spatial resolution (the HIRES region), and the more distant regions are modeled with a lower resolution,

global potential field (GLOBAL region). The size of the HIRES region is about 43° in longitude and 39° in latitude, and the spatial resolution in the low corona is $0.002 R_{\odot}$. The global field is constructed based on the SOLIS synoptic map, and the resolution is about 1° . Both HIRES and GLOBAL regions extend from the solar surface ($r = R_{\odot}$) up to a source surface ($r \sim 2 R_{\odot}$) where the magnetic field becomes radial. At the side boundaries of the HIRES domain, the magnetic field lines pass from the HIRES region into the GLOBAL region. The normal component of the magnetic field is continuous at these side boundaries. There may be small discontinuities in the tangential components at the side boundaries, but this has only minor effects on the magnetic field inside.

4.2. Stability of the Model

In our previous study, we find that the final result of the relaxation depends on the amount of the axial flux in the inserted flux rope. If this flux is not too large, the overlying arcade will be able to confine the expanding flux rope and the solution will reach a force-free equilibrium state: $\mathbf{j} \parallel \mathbf{B}$, so that $\mathbf{v} \rightarrow 0$. However, not all models will converge to a force-free state. If the axial flux exceeds a certain critical value Φ_{crit} , the flux rope will break through the overlying arcade and will continue to rise and expand. The value of Φ_{crit} can be determined by constructing a series of models with different values of Φ_{axi} but otherwise identical, and determining the outcome of the relaxation process. We find that the value of Φ_{crit} depends on the amount and distribution of the photospheric magnetic flux in the active region and on the selected path of the flux rope. Increasing the poloidal flux of the flux rope for a fixed axial flux can also produce instability. Hence, there are critical values for both the axial and poloidal fluxes.

If the axial flux or the poloidal flux is chosen to be slightly larger than the critical value, the expansion proceeds very slowly; this is due to the intrinsic slowness of the magneto-frictional relaxation. We find that it takes tens of thousands of iterations (time steps) to increase the height of the flux rope by a few Mm. Therefore, magneto-frictional relaxation is not suitable for simulating an eruption. However, it can be used to construct a model of the unstable state that exists at the early stage of the eruption. This is done by constructing a model with Φ_{axi} or F_{pol} that is slightly larger than the critical value and halting the relaxation process after some number of iterations (typically 30,000). The resulting field is not in equilibrium, but may provide a reasonable model for the marginally unstable state that exists at the onset of a flare/CME event. “Marginally unstable state” means a system at the boundary between stable and unstable states in parameter space. The model is based on the

Table 2
Parameters of Two Relaxation Methods

Relaxation 1				Relaxation 2			
Iteration	η_0	η_2	η_4	Iteration	η_0	η_2	η_4
0–20	0	0.1	0	0–100	1	0	0
20–100	1	0	0	100–1000	1	0	0.003
100–5000	1	0	0.01	1000–10000	1	0	0.001
5000–15000	1	0	0.003	10000–15000	1	0	0.0003
15000–20000	1	0	0.001	15000–20000	1	0	0.0003
20000–30000	1	0	0.0001	20000–30000	1	0	0.0001

idea that the magnetic field evolves from a stable configuration well before the flare to an unstable configuration after the flare started. Therefore, at the flare onset the field should be in a marginally unstable state.

Another constraint on the stability of the models is that the magnetic energy of the field after 30,000 iteration relaxations should be less than that of the open field. The latter is defined as the field in which all field lines from the active region are open, but those rooted in the surrounding quiet Sun may be closed. If the magnetic energy at the onset of a flare were larger than that of the open field, it would be difficult to understand how the configuration could evolve into such a state (eruptive instability would likely have occurred much sooner). To estimate the energy of the open field, we change the negative polarity

fields of the active region to positive polarity and then compute a potential field. The resulting open-field model has a magnetic energy $E_{\text{open}} = 8.3 \times 10^{31}$ erg, whereas the standard potential field has $E_{\text{pot}} = 5.29 \times 10^{31}$ erg. Therefore, the free energy of the open field is about 3.0×10^{31} erg. This requires that the free energy of the flux-rope models be less than 3.0×10^{31} erg.

4.3. Models for Different Axial and Poloidal Fluxes

We construct a grid of models in order to find the best-fit NLFFF model and the critical values of axial and poloidal fluxes. Two magneto-frictional relaxation methods are used in this study, and the parameters at different stages of the relaxation process for each method are shown in Table 2. η_2 and η_4 are given in dimensionless units related to the grid spacing and relaxation time step. The difference between the two relaxation methods is that in Relaxation 2 the second-order diffusion (η_2) is set to zero at all times, and the fourth-order diffusion (η_4) is reduced more quickly with iteration numbers, so that the poloidal flux of the flux rope is better preserved. Models 1–15 use Relaxation 1, while Relaxation 2 is used in the other 17 models. The model parameters are shown in Table 3. The first column of Table 3 refers to the model number, and the second and third columns show the input axial flux and the poloidal flux of the inserted flux rope. The fourth column presents the poloidal flux of the model after 30,000 iteration relaxations. The fifth column displays the

Table 3
Model Parameters for NOAA AR11060 and Comparisons with Pre-flare Loop Structures

Model No.	Φ_{axi} (10^{20} Mx)	F_{pol} (10^{10} Mx cm $^{-1}$)		Stable	X-point (Mm)	E_{free} (10^{31} erg)	$E_{\text{free}}/E_{\text{poten}}$ (%)	AD $^{\text{a}} \pm 0.2$ ($10^{-3} R_{\text{sun}}$)				
		Input	Final (± 0.2)					Loop 1	Loop 2	Loop 3	Loop 4	Loop 5
1	3	1	...	Y	N	0.88	17	3.2	2.9	3.2	1.2	3.0
2	4	1	...	Y	N	1.25	24	2.4	3.0	0.7	0.3	1.2
3	4.5	1	0.2	Y	N	1.43	27	2.2	3.0	0.5*	0.5*	0.7
4	5	1	1.1	?	4.2	1.6	30	2.2	4.1	0.7*	0.8*	0.3
5	6	1	1.5	N	8.4	1.89	36	2.6*	8.2	0.6*	2.1*	0.5
6	9	1	1.7	N	13.9	2.52	48
7	4.5	10	1.3	Y	N	1.89	36	6.4	3.9	0.6*	1.7*	2.3
8	5	10	2.3	?	4.2	2.09	40
9	6	10	2.9	N	8.4	2.42	46
10	4	0	...	Y	N	1.21	23	2.1	3.1	1.2	0.5	1.7
11	4	10	0.5	Y	N	1.68	32	6.6	3.8	1.1	1.0	2.1
12	4	20	1.4	Y	N	2.16	41
13	4	30	2.3	?	N	2.61	49
14	4	40	3.7	N	N	(3.05)	(58)
15	4	50	4.9	N	4.2	(3.48)	(66)
16	1	1	...	Y	N	0.55	10	8.9	5.7	4.4	3.6	6.0
17	2	1	0.2	Y	N	1.11	21	8.2	5.0	1.5	1.9	1.8
18	3	1	1.7	Y	N	1.62	31	7.4	5.8	0.4*	1.8*	1.6
19	4	1	3.1	?	N	2.06	39	4.7	2.9*	0.9*	1.2*	1.7
20	4.5	1	3.3	N	7.0	2.24	42
21	5	1	3.2	N	8.4	2.40	45
22	6	1	3.7	N	9.7	2.69	51
23	9	1	3.8	N	12.5	(3.34)	(63)
24	4.5	10	5.4	N	7.0	(3.39)	(64)
25	5	10	5.6	N	8.4	(3.62)	(68)
26	6	10	6.9	N	9.7	(3.99)	(75)
27	4	0	2.4	?	N	1.92	36	2.3	3.8*	1.0*	1.0*	1.2
28	4	10	5.2	N	N	(3.13)	(59)
29	4	20	7.5	N	5.6	(4.16)	(79)
30	4	30	8.8	N	12.5	(5.10)	(96)
31	4	40	10.3	N	14.0	(5.96)	(113)
32	4	50	11.4	N	18.1	(6.81)	(129)

Note. ^a Average deviation between observed loops and best-fit field lines from the model after 30,000 iteration relaxations.

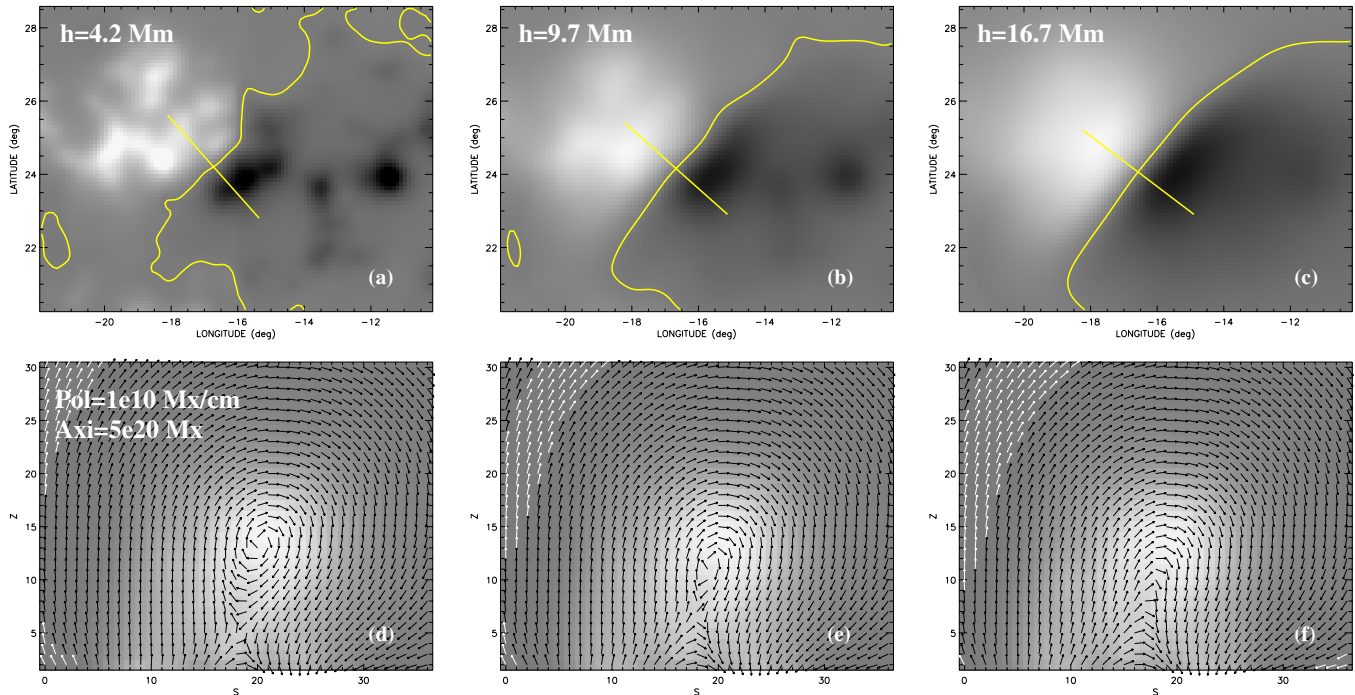


Figure 7. Magnetic fields and electric currents from Model 4 ($\Phi_{\text{axi}} = 5 \times 10^{20} \text{ Mx}$, $F_{\text{pol}} = 10^{10} \text{ Mx cm}^{-1}$). The top row presents the radial component of the magnetic fields from Model 4 at three different heights. The curved lines refer to the PILs. The bottom row displays the distribution of electric currents (grayscale image) and magnetic vectors at three different vertical slices. The axis unit in the bottom row is the cell size of our model (1 cell $\sim 1.4 \text{ Mm}$). The locations of these vertical planes are shown as the straight lines in the top row and are perpendicular to the PIL at the different heights. In order to show the vectors well, we use black arrows for brighter background and white arrows for darker background.

(A color version of this figure is available in the online journal.)

stability of the model, and the sixth column presents the height of the X-point (see below for the definition of the X-point) in the model after relaxation. The free energy of each model after 30,000 iteration relaxations is listed in the seventh column. The percentage of the free energy above the potential energy is listed in the eighth column. Note that the free energy in some unstable models (enclosed with brackets) is larger than that in the open field.

We first construct six models (Models 1–6) with a fixed poloidal flux (F_{pol}) of $10^{10} \text{ Mx cm}^{-1}$, and the axial fluxes in the flux rope of these models are 3, 4, 4.5, 5, 6, 9 in unit of 10^{20} Mx . Figure 7 shows magnetic fields and electric currents of Model 4, which is after 30,000 iteration relaxations. The radial components of the magnetic field at three different heights, panel (h), are shown on the top panels. The curved lines refer to the PIL. The bottom panels of Figure 7 show the electric currents' distribution in a vertical cross section of the flux rope, and the vectors refer to the magnetic vectors. In order to show the vectors well, we use black arrows for brighter background and white arrows for darker background. The location of the vertical plane is shown as straight lines in the corresponding top panels. These straight lines are crossing the same point at the PIL, and are perpendicular to the PIL at different heights. A visual inspection of the magnetic vectors in Figure 7(d) suggests two points at heights 5 and 14 cells (1 cell $\sim 1.4 \text{ Mm}$) where the projected magnetic field vanishes; these two points are called the X-point and the O-point, respectively. We call them the X-line and the O-line, when a 3D configuration is considered. The locations of the X-point and O-point depend on the projection plane. The height of the X-point is increased in Figure 7(e), and no clear X-point can be found in Figure 7(f). This figure shows that the distribution of the magnetic vectors

in the vertical cross section of the flux rope selected at different heights changes significantly. The effect of orienting the diagnostics plane in Figures 7(d)–(f) perpendicular to the PIL at different heights is a rotation of the plane (here counterclockwise). When the diagnostics plane is rotated, the main effect is that the axial field now has a component in this plane. Since the plane is rotated counterclockwise from Figure 7(d)–(f), this field component points from left to right in the whole part occupied by the flux rope. This reduces the vectors between the O-line and the X-line in the bottom half of the flux rope, which point from right to left (as one can clearly see in Figures 7(d)–(f)). By construction, the axial field is much stronger than the poloidal field, so that already a rather small projection of the axial component into the diagnostics plane (by a rather small rotation of the plane) leads to the unwanted dominance of the axial component in the plane. This result shows that in a realistic 3D magnetic configuration without translation symmetry, the exact location of the X-line cannot be precisely defined in practice. However, after testing on different models, we find that the distribution of the magnetic vectors and the electric currents closely match with each other, if the vertical cross section is selected at a special height, i.e., the height of the X-point. Therefore, later on the vertical slice of the flux rope is always selected at the height of the X-point, if there is one. For the models without an X-point, we use a fixed height of 4.2 Mm.

Figure 8 displays the distribution of electrical currents in a vertical cross section of the flux rope in Model 5 at different stages of the relaxation process. The iteration number is marked on the lower right corner of each panel. The grayscale image refers to the electric currents, and the vectors refer to the magnetic vectors. Note that these vectors circle around a point where the projected vectors vanish (i.e., O-point); this is also

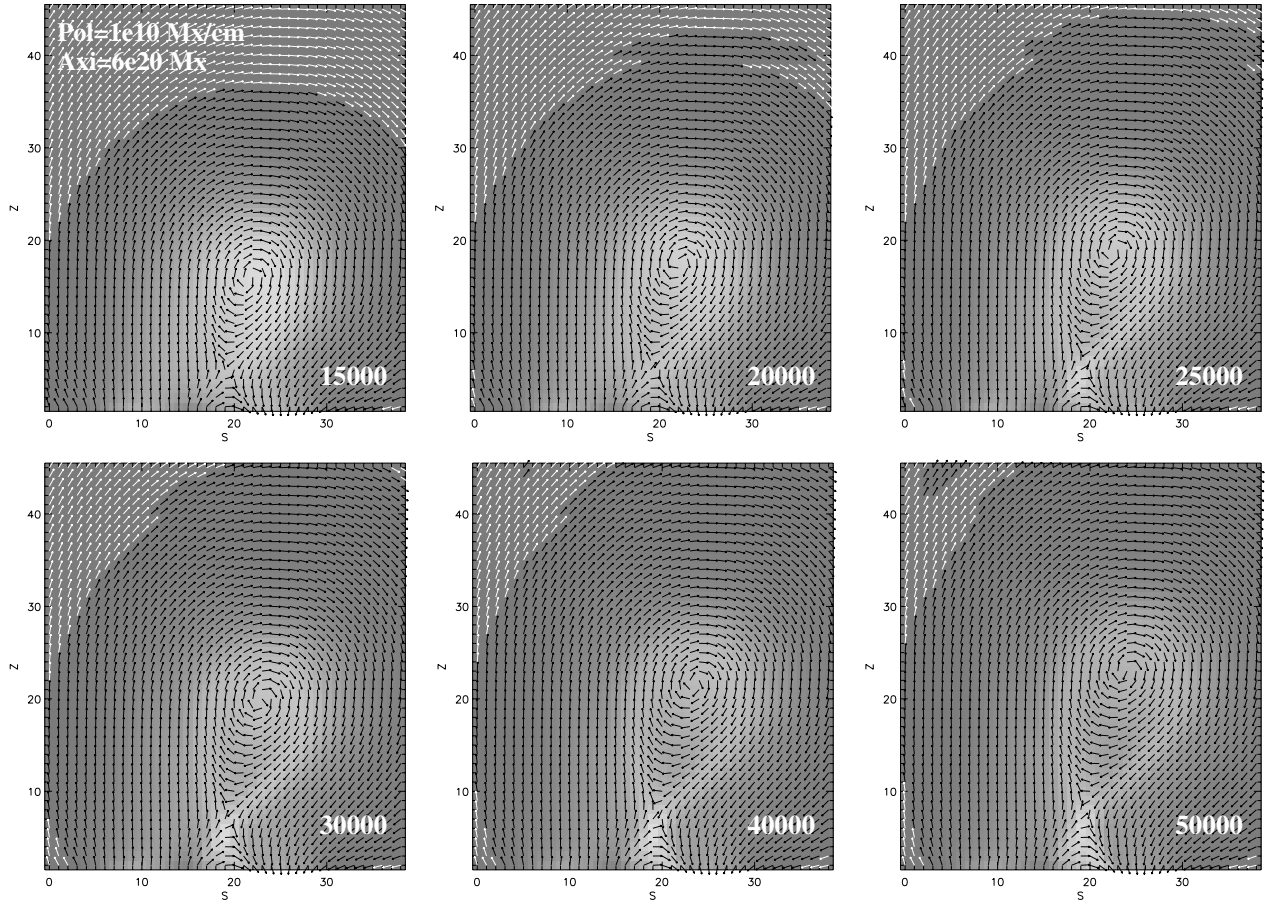


Figure 8. Vertical slices of the electric currents overlaid with magnetic vectors for Model 5 ($\Phi_{\text{axi}} = 6 \times 10^{20}$ Mx, $F_{\text{pol}} = 10^{10}$ Mx cm $^{-1}$) displayed at six different stages during the relaxation process. The iteration numbers are shown at the bottom right corner of each panel.

defined as the axis of the flux rope. This figure shows that the height of the axis of the flux rope increases with the iteration numbers. The flux rope is still expanding after 30,000 iteration relaxations, which suggests that this model is not a stable model.

Figure 9 shows the electric currents' distribution for different models after 30,000 iteration relaxations. Figure 9(a) shows the magnetic fields at a height of 4.2 Mm above the photosphere, and the straight line refers to the location of the vertical plane in Figures 9(b)–(d). The vertical planes in Figures 9(e) and (f) are selected at different heights as marked in the figure. No X-point can be found in the first two models with an axial flux of 3 and 4 ($\times 10^{20}$ Mx) as shown in Figures 9(b) and (c). The flux rope of these models relaxed to a force-free state after 30,000 iteration relaxations. An X-point appeared at the bottom of the flux rope in Model 4 (see Figure 9(d)), and the flux rope seems to be still expanding after 30,000 iteration relaxations. We refer to Model 4 as marginally stable, which is marked as “?” in Table 3. Figures 9(e) and (f) show a clear X-point, and the height of the X-point increases with the axial flux in the model. It is clear that these two models are unstable, because the flux ropes keep expanding even after 30,000 iteration relaxations. The electric current appears to be more concentrated at the boundary of the flux rope in Figures 9(e) and (f), possibly due to expansion of the flux rope and consequent misalignment of the magnetic field relative to that of the surrounding arcade. Therefore, the critical value of the axial flux is 5×10^{20} Mx, for a fixed F_{pol} of 10^{10} Mx cm $^{-1}$. We then construct three more models (Models 7–9) with a fixed F_{pol} of 10×10^{10} Mx cm $^{-1}$. Table 3 shows that

the critical value of the axial flux is still 5×10^{20} Mx. To find the critical poloidal flux, we construct six models (Models 10–15) with a fixed Φ_{axi} of 4×10^{20} Mx, and the poloidal fluxes of these models are 0, 10, 20, 30, 40, 50 in units of 10^{10} Mx cm $^{-1}$. We find that the critical value of the poloidal flux is 30×10^{10} Mx cm $^{-1}$.

The final poloidal fluxes listed in the fourth column of Table 3 are measured by integrating the flux between the center of the flux rope and the X-line (or height 2.8 Mm above the photosphere for the models without an X-line) for models after 30,000 iteration relaxations. The center of the flux rope refers to the center of the magnetic vectors in the flux rope, which is marked as a plus symbol in the bottom panels of Figure 9. A “...” symbol is listed for the models without a center of the flux rope. Among the models that we construct, there are three types of magnetic configurations: sheared arcade; flux rope without an X-line; flux rope with an X-line. We find that the axial flux and/or the poloidal flux in the models with a sheared arcade are the smallest, the latter two types of configurations appear sequentially by increasing the axial flux and/or the poloidal flux. The final poloidal fluxes are only measured for the latter two types of models. Table 3 shows that the final F_{pol} of the flux rope is much smaller than the input amount for most of the 15 models. This suggests that the poloidal flux of the flux rope is significantly reduced during the magneto-frictional relaxation process. This effect is more clearly seen in the models with a larger input poloidal flux. Table 3 shows that the final poloidal fluxes in Models 4–6 are larger than the input amounts, which may be due to the contribution of a newly reconnected magnetic

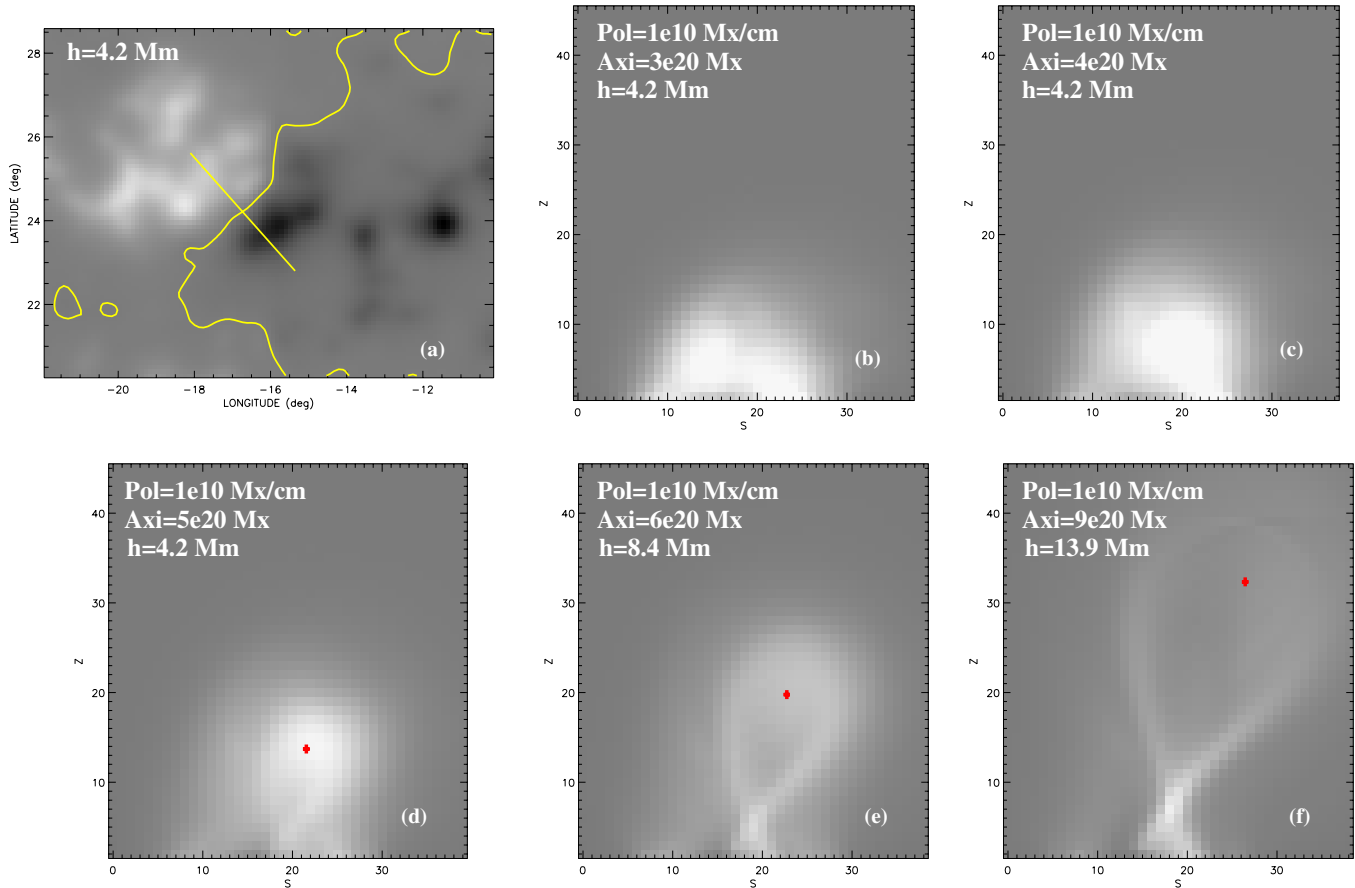


Figure 9. (a) Radial component of the magnetic fields at height 4.2 Mm from the model shown in panel (b). (b)–(f) Vertical slices of electric currents for five different models (Model) after 30,000 iteration relaxations. The locations of the vertical slices are represented as the straight line in panel (a). The plus symbol refers to the center of the magnetic vectors in the flux rope.

(A color version of this figure is available in the online journal.)

flux. The final poloidal flux is also increasing with the axial flux in the model. Because the height of the X-line is increasing, more and more reconnected magnetic fluxes contribute to the final F_{pol} .

All of the 15 models described above are created using Relaxation 1. In these models, we find that the poloidal fluxes are significantly reduced during the relaxation process. To understand how a different relaxation process will affect the reduction of the poloidal flux, 17 models (Models 16–32) are created using Relaxation 2. We find that Relaxation 2 preserves the poloidal flux better than Relaxation 1. A detailed comparison between Relaxation 1 and Relaxation 2 can be found in the [Appendix](#). A diagram of the threshold of stability for the above-mentioned models is presented in Figure 10. This figure shows that the models using Relaxation 2 have lower critical values than the models using Relaxation 1.

4.4. Comparison with Observations

In this section, we will compare our models with observations to find the best-fit NLFFF model prior to the flare. Furthermore, we will explore how well our unstable model matches the observations at the early stage of the flare.

4.4.1. Model Prior to the Flare

Figure 11 shows EUV (193 Å, left and right) and X-ray (Ti-poly, middle) images observed by *SDO/AIA* and *Hinode/XRT* prior to the flare. The red and green contours refer to the

positive and negative magnetic fields observed by *SDO/HMI*. Five coronal loops (red lines in Figures 11(a) and (b)) are selected from observations to constrain the pre-flare model. Two loops at the upper part of the region are selected from the AIA images (Figure 11(a)), and three loops at the bottom are selected based on the XRT observations (Figure 11(b)). The method for finding the best-fit model field line for a particular observed loop is described in detail in Su et al. (2009a). We define the “average deviation” (AD) between an observed loop and a model field line by measuring the distance between a point on the observed loop and the closest point on the projected field line in the image plane, and then averaging these distances for various points along the observed loop. The AD between an observed loop and the best-fit model field line from each model is listed in the last five columns of Table 3.

A comparison of the ADs for Models 1–5 suggests that Models 2 and 3 appear to be the best-fit models. However, for loops 3 and 4 in Model 3 the best-fit field lines do not fit the observed loop very well because the field lines are much longer than the observed loops. The reason is that the AD is measured from a point on the loop to the nearest point on the projected field line, so parts of the field line that extends beyond the observed loop are not taken into account in the AD measurement, but nevertheless indicate disagreement with the observations. These field lines are marked with a “*” symbol. The ADs for Model 6 are not provided because it is clear that this model fits the observations poorly. Therefore, for a fixed

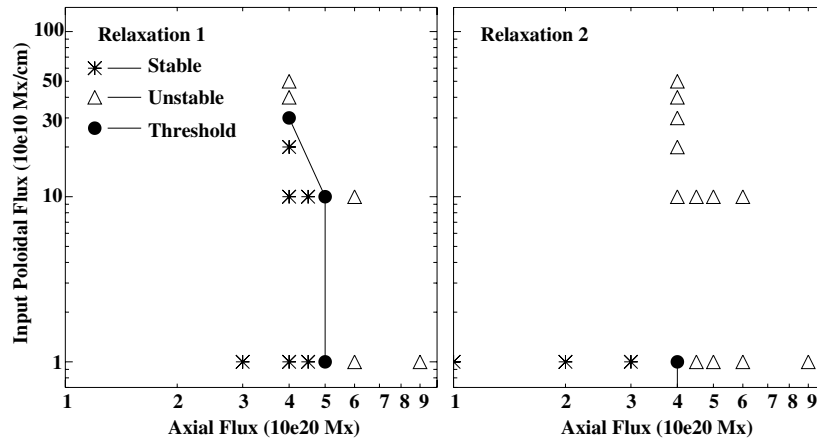


Figure 10. Diagram of the threshold of instability for models with two relaxation methods. Note that Models 10 and 24 are not displayed in this plot.

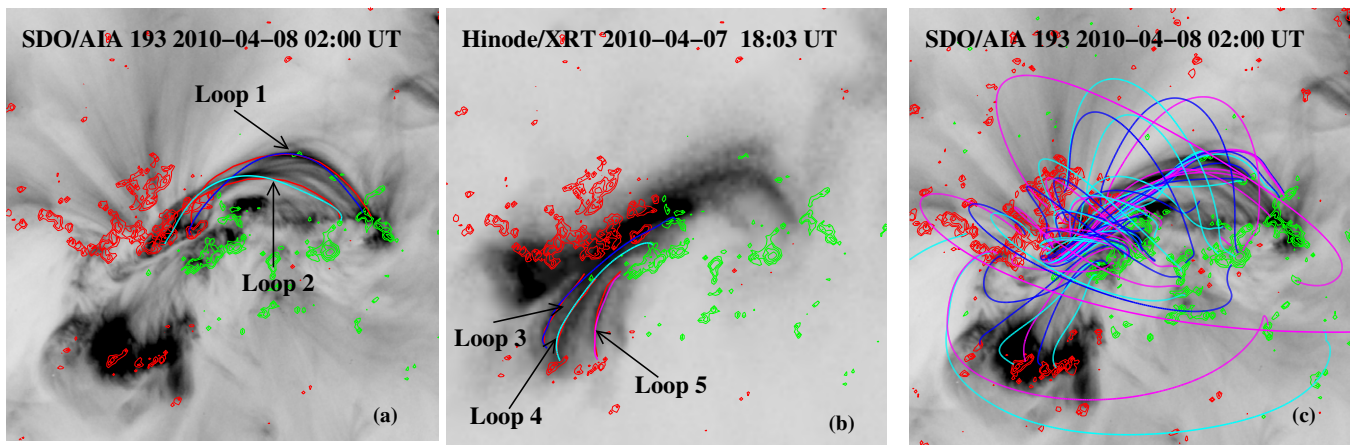


Figure 11. (a) and (b) *SDO/AIA* and *Hinode/XRT* images of the flaring region prior to the event. *SDO/HMI* magnetic field observations are presented as red and green contours. The red lines refer to the five manually traced coronal loops, and the other color lines are the best-fit model field lines from Model 2. (c) Selected field lines from Model 2 overlaid on the *SDO/AIA* image prior to flare. The field of view of each panel is $0.25 R_{\odot}$.

poloidal flux of $10^{10} \text{ Mx cm}^{-1}$, the best-fit model has an axial flux of $4 \times 10^{20} \text{ Mx}$. This model is an NLFFF model, and the axial flux in this model is very close to the threshold of instability ($5 \times 10^{20} \text{ Mx}$). For a fixed axial flux of $4 \times 10^{20} \text{ Mx}$, both models with a poloidal flux of 0 (Model 10) and $10^{10} \text{ Mx cm}^{-1}$ (Model 2) show good fit to the observations, and the latter model shows slightly better fit. If the poloidal flux is increased to $10 \times 10^{10} \text{ Mx cm}^{-1}$ (Model 11), the fit gets worse. Hence, for models with a fixed axial flux of $4 \times 10^{20} \text{ Mx}$, the best-fit model has a poloidal flux of $10^{10} \text{ Mx cm}^{-1}$, which is far away from the threshold of instability ($30 \times 10^{10} \text{ Mx cm}^{-1}$). Moreover, the best-fit model using Relaxation 1 shows better fit to the observations than that using Relaxation 2 (for details, see the [Appendix](#)). Therefore, we will only consider the models with Relaxation 1 in the following section.

In summary, the best-fit pre-flare model that we construct is Model 2, which is marked by bold fonts in Table 3. The five color field lines in Figures 11(a) and (b) refer to the best-fit field lines from this model to the observed coronal loops. This figure suggests that this model matches the observations very well. Although the field lines in Figure 11(b) extend slightly farther than the observed loops were drawn, this does not contradict our work. We expect the coronal loops to be longer, but are unable to draw them accurately after a certain region of the image due to saturation. More selections of field lines from this model are shown in Figure 11(c), which suggests that this model contains a highly sheared and weakly twisted flux rope.

4.4.2. Model at the Early Stage of the Flare

As mentioned in previous sections, the model will become unstable, if we increase the axial flux or the poloidal flux over the threshold of instability. The distribution of electric currents and magnetic fields in these models (Figures 7 and 8) presents a reconnection topology which is similar to the standard flare models. Therefore, we expect that our models that just pass the threshold of instability should match the observations at the early stage of the flare.

Figure 12 shows comparisons of AIA observations of the flare with Model 5, in which the axial flux passes the threshold of instability. Figure 12(a) depicts the flare loops observed at 94 \AA at the early phase of the flare. The red and green contours refer to the positive and negative magnetic polarities observed by *SDO/HMI*. Figure 12(b) presents the same grayscale image as that in Figure 12(a). A vertical cross section of the electric currents' distribution from Model 5 is shown in Figure 12(c). The locations where the field lines cross the vertical plane are marked as white circles. The color field lines in Figure 12(b) are the newly reconnected field lines that are located below the reconnection point as shown in Figure 12(c). Figure 12(b) suggests that these reconnection field lines are highly sheared and match the observed flare loops very well. This is consistent with the standard interpretation of the flare loops. The coronal dimming regions are clearly seen at 193 \AA shown in Figures 12(d) and (e). The background image in Figure 12(f) is the same as

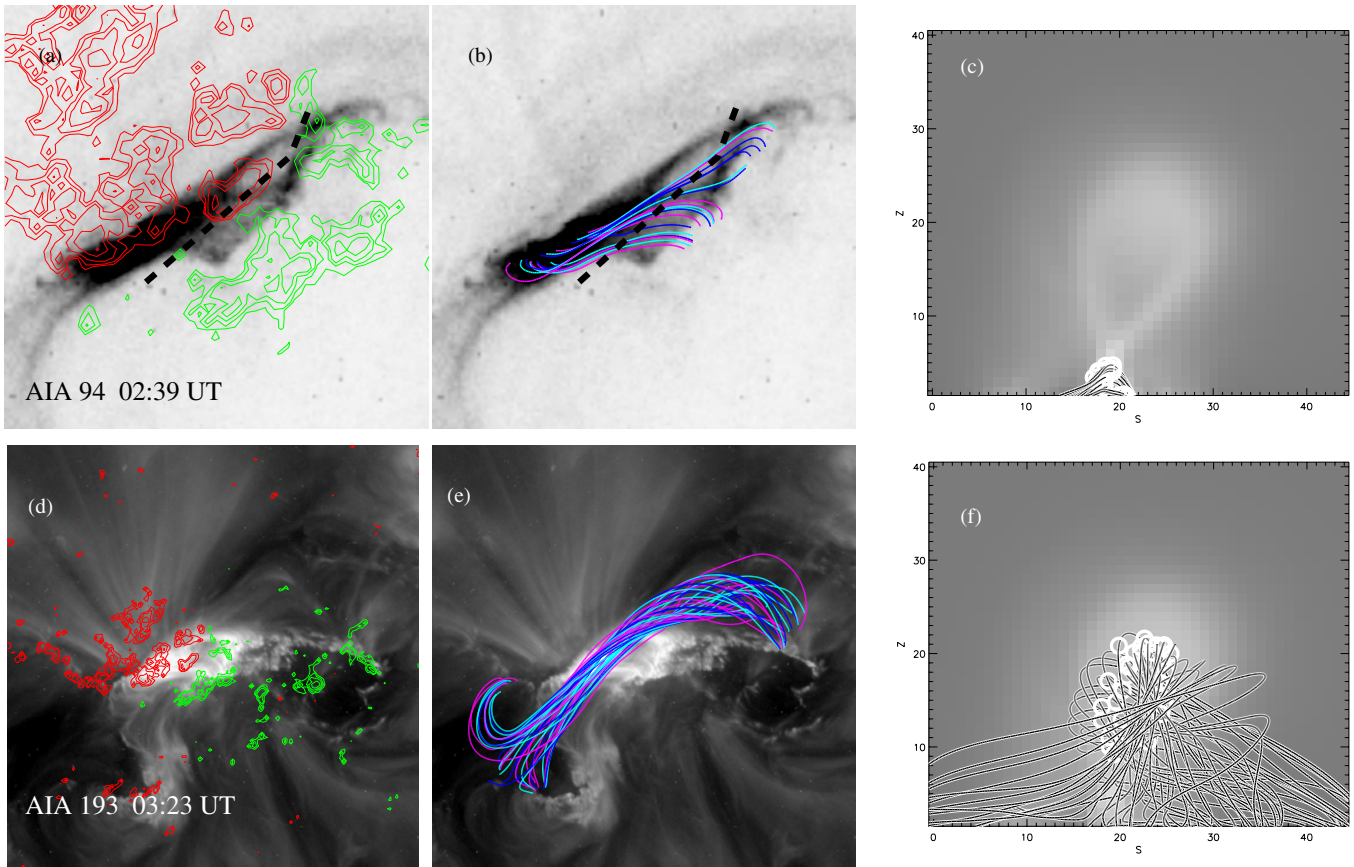


Figure 12. AIA image at 94 \AA taken at 02:39 UT is shown in panels (a) and (b). The red and green contours refer to the positive and negative magnetic fields observed by *SDO/HMI* at 02:00 UT. The black dashed lines represent the PIL. The color lines in panel (b) are the field lines from Model 5. (c) Vertical slice of electric currents of Model 5, and the field lines are the same as in panel (b). The white circles refer to the location where the field lines are crossing the vertical plane. (d) and (e) AIA image at 193 \AA taken at 03:23 UT. (f) The same current plot as panel (c). The field lines in panels (e) and (f) are also from Model 5. The field of view of images in panels (d) and (e) ($0.25 R_{\odot}$) is about three times of that in panels (a) and (b) ($0.08 R_{\odot}$).

that in Figure 12(c). The crossing points of the color field lines from Figure 12(e) are located above the reconnection point. These field lines are supposed to represent the erupting flux rope. Figure 12(e) shows that the erupting flux rope is still weakly twisted at this stage, and the footpoints of this flux rope are located around the coronal dimming regions. This is also consistent with the current understanding of coronal dimmings, which are the footpoints of the erupting flux rope.

The poloidal flux in Model 14 just passes the threshold of instability, but the magnetic free energy in this model is very close to the free energy in the open field. Therefore, Figure 13 shows comparisons of AIA flare observations with Model 13, in which the poloidal flux is at the threshold of instability. Figure 13(a) suggests that the footpoints of the erupting flux rope are also located around the coronal dimming regions, which is similar to Model 5. But the two footpoints of the erupting flux rope in Model 13 are bulging out in comparison with Model 5. As far as we are aware, this had never been observed in erupting filaments and never been in published CME simulations (B. Kliem 2011, private communication). Unlike Model 5, no clear X-point can be found in the vertical cross sections of the current plot as shown in Figure 13(b). Therefore, no field lines from Model 13 can match the flare loops. The location of the erupting flux rope's footpoints may depend on the path that we selected to insert the flux rope. It is not surprising that the footpoints of the erupting flux rope in both Models 5 and 13 are located at the same regions. As mentioned in the

last section, the axial flux in the best-fit model is very close to the threshold, while the poloidal flux is still far away from the threshold. Therefore, we think that the unstable model due to increase of the axial flux is more reasonable for the early phase of the flare.

5. SUMMARY AND DISCUSSION

We study a solar eruption that occurred in AR 11060 on 2010 April 8. This event involves: two-ribbon flare, slow CME, filament eruption, EIT wave, and coronal dimmings. *SDO/AIA* and *STEREO/EUVI* observations show that the event begins with a nearly horizontal filament ejection along the internal PIL from the north to the south around 02:10 UT. About 18 minutes later, the internal filament starts to lift off, which is associated with highly sheared flare brightenings located on the two sides of the internal filament. The AIA 94 \AA (Fe XVIII) channel first observes the highly sheared flare loops connecting the first flare brightenings. At the end of the event, the active region displays nearly potential post-flare loops. This strong to weak shear change of the flare footpoints/loops is consistent with our previous findings (Su et al. 2006, 2007a).

In order to find the best-fit pre-flare model and the unstable model for the early stage of the event, we construct a grid of models using two relaxation methods. Models 1–15 are created with different axial and poloidal fluxes using Relaxation 1, while Relaxation 2 is used for Models 16–32. We find that the input

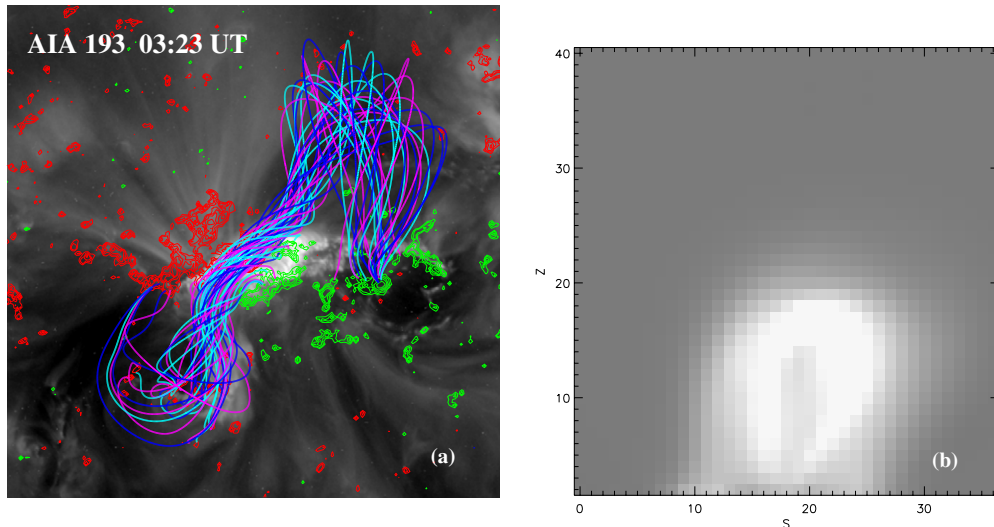


Figure 13. (a) Selected field lines from Model 13 overlaid on the same AIA images at 193 Å as shown in Figure 12. The field of view is $0.3 R_{\odot}$. (b) Vertical slice of electric currents from Model 13.

poloidal flux is significantly reduced during the 30,000 iteration relaxations process for most models. This may explain why the poloidal flux is always very difficult to constrain in our previous work. Relaxation 2 appears to preserve the poloidal flux slightly better than Relaxation 1. This fact may explain why the threshold of instability for both axial and poloidal fluxes in models using Relaxation 1 is larger than that using Relaxation 2. We also find that the best-fit model using Relaxation 1 matches the observed coronal loops better than that using Relaxation 2. Therefore, all of the results discussed below are from the models using Relaxation 1.

We find that the best-fit pre-flare NLFFF model ($\Phi_{\text{axi}} = 4 \times 10^{20} \text{ Mx}$, $F_{\text{pol}} = 10^{10} \text{ Mx cm}^{-1}$) contains a highly sheared and weakly twisted flux rope. The free energy in this model is $1.25 \times 10^{31} \text{ erg}$, which is about 24% of the potential energy ($5.29 \times 10^{31} \text{ erg}$). For a fixed F_{pol} of $10^{10} \text{ Mx cm}^{-1}$, the axial flux in the best-fit model is close to the threshold of instability ($5 \times 10^{20} \text{ Mx}$). However, the poloidal flux in the best-fit model is still far away from the critical value ($30 \times 10^{10} \text{ Mx cm}^{-1}$), for a fixed Φ_{axi} of $4 \times 10^{20} \text{ Mx}$. The total unsigned flux in this active region is $3.7 \times 10^{21} \text{ Mx}$. Therefore, the axial flux of $4 \times 10^{20} \text{ Mx}$ in the best-fit model corresponds to 22% of the average unsigned flux of the active region. This result is larger than our previous modeling results ($\sim 10\% - 14\%$) as summarized by Green et al. (2011). We estimate the field line turns in the model (Model 13) with $\Phi_{\text{axi}} = 4 \times 10^{20} \text{ Mx}$ and the critical poloidal flux ($30 \times 10^{10} \text{ Mx cm}^{-1}$). The estimation is based on the following equation: $N = F_{\text{pol}} \times L / \Phi_{\text{axi}}$. Here L is the length of the flux rope’s axis, which is estimated by the length of a randomly selected field line in the center of the flux rope. This length is about 267.4 Mm. We use the final poloidal flux ($2.3 \times 10^{10} \text{ Mx cm}^{-1}$) in this calculation, since the input poloidal flux is significantly reduced during the magneto-relaxation process. Therefore, our estimated number of field line turns in this model is about 1.5. Hence, the twist of the flux rope in this model is about 3.0π , according to the equation $\phi_{\text{twist}} = 2\pi \times N$. This number is smaller than the critical twist (3.5π) for kink instability in the numerical modeling in more idealized configurations (e.g., Fan & Gibson 2003, 2004; Gibson et al. 2004; Kliem et al. 2004; Török et al. 2004).

We choose two unstable models to compare with observations of the flare: one is due to increase of the axial flux (Model 5: $\Phi_{\text{axi}} = 6 \times 10^{20} \text{ Mx}$, $F_{\text{pol}} = 10^{10} \text{ Mx cm}^{-1}$), and the other one is due to increase of the poloidal flux (Model 13: $\Phi_{\text{axi}} = 4 \times 10^{20} \text{ Mx}$, $F_{\text{pol}} = 30 \times 10^{10} \text{ Mx cm}^{-1}$). The vertical cross sections of electric currents and magnetic fields in Model 5 display a clear X-point, indicating a reconnection topology. According to the standard “CSHKP” model, the field lines above the X-point represent the erupting flux rope, while the field lines below the X-point refer to the newly formed flare loops. For Model 5, we find that the reconnected field lines below the X-point closely match the observed highly sheared flare loops at the early stage of the flare, but no X-point is identified in Model 13. For both unstable models, the footpoints of the erupting flux rope are located around the two dimming regions. But the erupting flux rope in Model 13 is bulging out at both ends, which has never been observed. As mentioned in the last paragraph, the axial flux in the best-fit model is very close to the threshold, while the poloidal flux is still far away from the threshold. Therefore, we think that the unstable model due to increase of axial flux is more reasonable for the early phase of the flare.

In this paper, we assumed that the target active region is already close to the unstable state when the flare occurs. In this case, the eruption may be due to the loss of equilibrium of the magnetic configuration, or may be triggered by some sudden external event that is not very energetic. We find that the unstable model fits the observed flare loops quite well, which is consistent with our assumption. There is no need for a sudden external trigger that is very energetic, and indeed none is observed. The nearly horizontal filament ejection that occurred around 20 minutes before the flare onset suggests that this event may be initiated by ideal catastrophic loss of equilibrium. The modeling results suggest that this loss of equilibrium may be caused by the increase of the axial flux of the flux rope. Loss of equilibrium could be driven by flux emergence, flux cancellations, footpoint motions, and so on. For the event under study, frequent flux cancellations at the internal PIL prior to the eruption are observed by *SDO/HMI*. Comprehensive observational studies (e.g., Green et al. 2011; Sterling et al. 2010) have demonstrated that flux cancellations

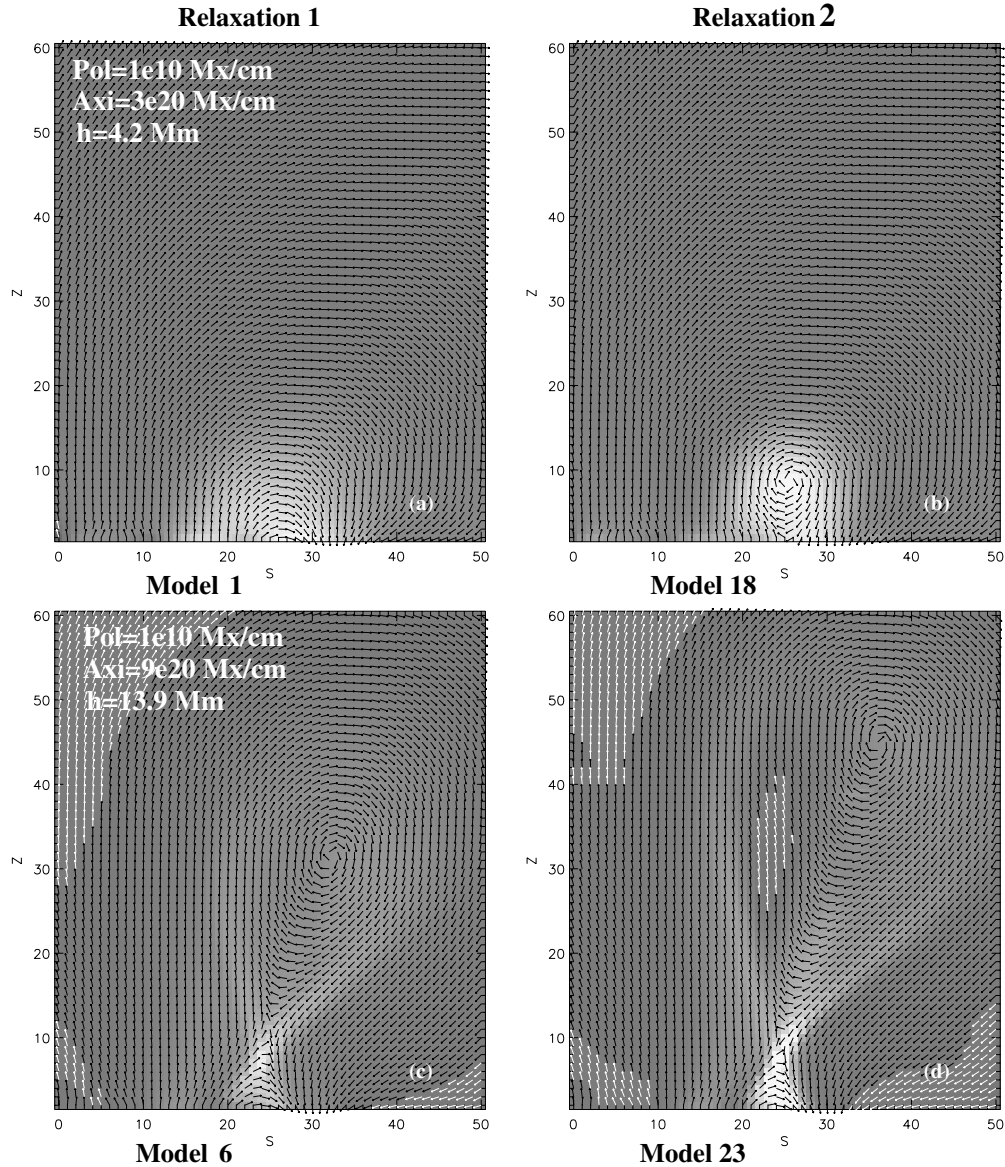


Figure 14. Comparisons of vertical slices of electric currents and magnetic vectors from models with two different relaxation methods.

could trigger eruptions. Therefore, this event may be initiated by ideal catastrophic loss of equilibrium caused by increase of the axial flux in the flux rope, which is driven by flux cancellations. However, without a more comprehensive study, we cannot conclude that this is the only possible initiation mechanism for this event.

Our models are constructed based on a high-resolution *SDO*/HMI magnetogram. They are empirical models which are constrained by an observed filament and coronal loops. The advantage of our approach is that the models are very realistic and have very high spatial resolution ($0.002 R_{\odot}$). However, there are also limitations of our model. We are not able to see long current sheets in our unstable model, because our diffusion is too large to allow the existence of a long current sheet. In our unstable model, the expansion of the flux rope proceeds very slowly; this is due to the intrinsic slowness of magneto-frictional relaxation. We find that it takes tens of thousands of iterations (time steps) to increase the height of the flux rope by a few Mm. Therefore, magneto-frictional relaxation is not suitable for simulating an eruption. To model the entire eruption process,

one needs a full 3D MHD simulation, and our unstable models can be used as initial conditions.

We thank Dr. Bernhard Kliem and the anonymous referee for reading the manuscript, and we greatly appreciate their valuable comments that significantly improved this paper. Y.S. is grateful to Drs. Paolo Grigis and Kathy Reeves for help with data processing and thanks Mr. Alexander Engell for a useful conversation. *Hinode* is a Japanese mission developed and launched by ISAS/JAXA, with NAOJ as a domestic partner and NASA and STFC (UK) as international partners. It is operated by these agencies in cooperation with ESA and the NSC (Norway). We thank the teams of *SDO*/AIA, *SDO*/HMI, *STEREO*/SECCHI, *Hinode*/XRT, KSO, *SOHO*/LASCO, *GOES*, and *SOLIS* for providing the valuable data. The *STEREO* and HMI data are downloaded via the Virtual Solar Observatory and the Joint Science Operations Center. This paper uses data from the CACTus CME catalog, generated and maintained by the SIDC at the Royal Observatory of Belgium. This project is partially supported under contract NNM07AB07C from

NASA to the Smithsonian Astrophysical Observatory (SAO) and SPO2H1701R from LMSAL to SAO. V.S. is supported under the NSF-REU solar physics program at SAO, grant number ATM-0851866.

APPENDIX

COMPARISON OF THE TWO RELAXATION PROCESSES

As mentioned in Section 4.3, Models 1–15 are created using Relaxation 1. Using the same parameters as Models 1–15, Models 18–32 are created with a different relaxation process, i.e., Relaxation 2. The difference between these two relaxation processes can be found in Table 2. Table 3 shows that the final F_{pol} in the models using Relaxation 2 is larger than that in the corresponding models using Relaxation 1. This suggests that Relaxation 2 preserves the poloidal flux better than Relaxation 1. Similar to Relaxation 1, Relaxation 2 also reduces the poloidal flux significantly, which can be clearly identified in Models 24–32 except Model 27. Note that the final poloidal flux in Models 18–19 and 27 is larger than the input amount, and these models show no clear evidence of reconnection. This may be due to the fact that the cross section is not selected properly, and some axial flux of the flux rope is taken into account. As indicated in Figure 7, a slight change in the selection of the cross section could result in significant changes in the measurements of the final poloidal flux.

Figure 14 presents vertical cross sections of electric currents and magnetic vectors for models using two relaxation methods. The maximum strength of the currents in each image is the same. As shown in Figure 14(b), the model with Relaxation 2 displays a flux rope with a clear center in the magnetic vectors, while the model with Relaxation 1 presents a sheared-arcade configuration (Figure 14(a)). A comparison of Figures 14(c) and (d) suggests that the flux rope above the X-point in the model with Relaxation 2 is larger and higher than that in the model with Relaxation 1. Moreover, the current below the X-point in the model with Relaxation 2 is also stronger. This result is consistent with the fact that Relaxation 2 preserves the poloidal flux better than Relaxation 1.

As shown in Table 3, the critical value of the axial flux in the model using Relaxation 2 is smaller than that using Relaxation 1. Therefore, we create two more models with a smaller axial flux, in order to find the best-fit model. For all the models using Relaxation 2 (Models 16–32), the poloidal and axial fluxes in the best-fit model (Model 17) are $10^{10} \text{ Mx cm}^{-1}$ and $2 \times 10^{20} \text{ Mx}$, respectively. In comparison with the corresponding models with Relaxation 1, the axial flux in Model 17 is slightly farther away from the threshold of instability ($4 \times 10^{20} \text{ Mx}$). The axial flux in Model 17 is only half of that in Model 2, which is the best-fit model using Relaxation 1. Moreover, the ADs also suggest that the best-fit model using Relaxation 2 is worse than that using Relaxation 1.

REFERENCES

- Amari, T., Luciani, J. F., Aly, J. J., Mikic, Z., & Linker, J. 2003a, *ApJ*, **585**, 1073
- Amari, T., Luciani, J. F., Aly, J. J., Mikic, Z., & Linker, J. 2003b, *ApJ*, **595**, 1231
- Antiochos, S. K., Dahlburg, R. B., & Klimchuk, J. A. 1994, *ApJ*, **420**, L41
- Antiochos, S. K., DeVore, C. R., & Klimchuk, J. A. 1999, *ApJ*, **510**, 485
- Bisi, M. M., et al. 2010, *Sol. Phys.*, **265**, 49
- Bobra, M. G., van Ballegoijen, A. A., & DeLuca, E. E. 2008, *ApJ*, **672**, 1209
- Brueckner, G. E., et al. 1995, *Sol. Phys.*, **162**, 357
- Burlaga, L. F. E. 1991, *Physics of the Inner Heliosphere II* (Berlin: Springer), 1
- Canfield, R. C., Hudson, H. S., & McKenzie, D. E. 1999, *Geophys. Res. Lett.*, **26**, 627
- Canou, A., & Amari, T. 2010, *ApJ*, **715**, 1566
- Chen, P. F., & Shibata, K. 2000, *ApJ*, **545**, 524
- Cheng, X., Ding, M. D., Guo, Y., Zhang, J., Jing, J., & Wiegelmann, T. 2010, *ApJ*, **716**, L68
- Cohen, O., Attrill, G. D. R., Manchester, W. B., & Wills-Davey, M. J. 2009, *ApJ*, **705**, 587
- Cohen, O., Attrill, G. D. R., Schwadron, N. A., Crooker, N. U., Owens, M. J., Downs, C., & Gombosi, T. I. 2010, *J. Geophys. Res. (Space Phys.)*, **115**, 10104
- Fan, Y., & Gibson, S. E. 2003, *ApJ*, **589**, L105
- Fan, Y., & Gibson, S. E. 2004, *ApJ*, **609**, 1123
- Fan, Y., & Gibson, S. E. 2007, *ApJ*, **668**, 1232
- Forbes, T. G. 1990, *J. Geophys. Res.*, **95**, 11919
- Forbes, T. G., & Isenberg, P. A. 1991, *ApJ*, **373**, 294
- Forbes, T. G., Priest, E. R., & Isenberg, P. A. 1994, *Sol. Phys.*, **150**, 245
- Fuhrmann, M., Seehafer, N., Valori, G., & Wiegelmann, T. 2011, *A&A*, **526**, A70
- Gibson, S. E., Fan, Y., Mandrini, C., Fisher, G., & Demoulin, P. 2004, *ApJ*, **617**, 600
- Gibson, S. E., & Low, B. C. 1998, *ApJ*, **493**, 460
- Golub, L., et al. 2007, *Sol. Phys.*, **243**, 63
- Green, L. M., Kliem, B., & Wallace, A. J. 2011, *A&A*, **526**, A2
- Guo, Y., Schmieder, B., Démoulin, P., Wiegelmann, T., Aulanier, G., Török, T., & Bommier, V. 2010, *ApJ*, **714**, 343
- Howard, R. A., et al. 2008, *Space Sci. Rev.*, **136**, 67
- Kano, R., et al. 2008, *Sol. Phys.*, **249**, 263
- Kliem, B., Titov, V. S., & Török, T. 2004, *A&A*, **413**, L23
- Kosugi, T., & Acton, L. W. 2002, in *Multi-Wavelength Observations of Coronal Structure and Dynamics—Proc. Yohkoh 10th Anniversary Meeting*, ed. P. C. H. Martens & D. Cauffman (COSPAR Colloquia Series; Amsterdam: Elsevier), 7
- Kosugi, T., et al. 2007, *Sol. Phys.*, **243**, 3
- Krall, J., Chen, J., & Santoro, R. 2000, *ApJ*, **539**, 964
- Lemen, J. R., et al. 2011, *Sol. Phys.*, submitted
- Lin, J., & Forbes, T. G. 2000, *J. Geophys. Res.*, **105**, 2375
- Linker, J. A., Lionello, R., Mikić, Z., & Amari, T. 2001, *J. Geophys. Res.*, **106**, 25165
- Linker, J. A., & Mikic, Z. 1995, *ApJ*, **438**, L45
- Liu, W., Nitta, N. V., Schrijver, C. J., Title, A. M., & Tarbell, T. D. 2010, *ApJ*, **723**, L53
- Low, B. C., Fong, B., & Fan, Y. 2003, *ApJ*, **594**, 1060
- Lynch, B. J., Antiochos, S. K., DeVore, C. R., Luhmann, J. G., & Zurbuchen, T. H. 2008, *ApJ*, **683**, 1192
- Manchester, W. 2003, *J. Geophys. Res. (Space Phys.)*, **108**, 1162
- Manchester, W. B., Gombosi, T. I., Roussev, I., De Zeeuw, D. L., Sokolov, I. V., Powell, K. G., Tóth, G., & Opher, M. 2004, *J. Geophys. Res. (Space Phys.)*, **109**, 1102
- Manchester, W. B., IV, et al. 2008, *ApJ*, **684**, 1448
- Martin, S. F. 1998, *Sol. Phys.*, **182**, 107
- Mikic, Z., & Linker, J. A. 1994, *ApJ*, **430**, 898
- Moore, R., et al. 1980, *SkyLab Solar Workshop II* (Boulder, CO: Colorado Associated Univ. Press), 341
- Moore, R. L., Sterling, A. C., Hudson, H. S., & Lemen, J. R. 2001, *ApJ*, **552**, 833
- Priest, E. R., & Forbes, T. G. 2002, *A&ARv*, **10**, 313
- Reeves, K. K., & Golub, L. 2011, *ApJ*, **727**, L52
- Robbrecht, E., Berghmans, D., & Van der Linden, R. A. M. 2009, *ApJ*, **691**, 1222
- Roussev, I. I., Forbes, T. G., Gombosi, T. I., Sokolov, I. V., DeZeeuw, D. L., & Birn, J. 2003, *ApJ*, **588**, L45
- Rust, D. M., & Kumar, A. 1996, *ApJ*, **464**, L199
- Rust, D. M., & LaBonte, B. J. 2005, *ApJ*, **622**, L69
- Savcheva, A., & van Ballegoijen, A. 2009, *ApJ*, **703**, 1766
- Schou, et al. 2011, *Sol. Phys.*, submitted
- Sterling, A. C., Chifor, C., Mason, H. E., Moore, R. L., & Young, P. R. 2010, *A&A*, **521**, A49
- Su, Y., Golub, L., & Van Ballegoijen, A. A. 2007a, *ApJ*, **655**, 606
- Su, Y., et al. 2007b, *PASJ*, **59**, 785
- Su, Y., van Ballegoijen, A., Lites, B. W., Deluca, E. E., Golub, L., Grigis, P. C., Huang, G., & Ji, H. 2009a, *ApJ*, **691**, 105
- Su, Y., van Ballegoijen, A., Schmieder, B., Berlicki, A., Guo, Y., Golub, L., & Huang, G. 2009b, *ApJ*, **704**, 341
- Su, Y. N., Golub, L., van Ballegoijen, A. A., & Gros, M. 2006, *Sol. Phys.*, **236**, 325

- Svestka, Z., & Cliver, E. W. 1992, in IAU Colloq. 133, Vol. 399, Eruptive Solar Flares, ed. Z. Svestka, B. V. Jackson, & M. E. Machado (New York: Springer), 1
- Tang, F. 1985, *Sol. Phys.*, **102**, 131
- Thompson, B. J., Cliver, E. W., Nitta, N., Delannée, C., & Delaboudinière, J.-P. 2000, *Geophys. Res. Lett.*, **27**, 1431
- Titov, V. S., Mikic, Z., Linker, J. A., & Lionello, R. 2010, AGU Fall Meeting Abstracts, SH51C-1687
- Török, T., Kliem, B., & Titov, V. S. 2004, *A&A*, **413**, L27
- van Ballegooijen, A. A. 2004, *ApJ*, **612**, 519
- van Ballegooijen, A. A., & Martens, P. C. H. 1989, *ApJ*, **343**, 971
- van Ballegooijen, A. A., Priest, E. R., & Mackay, D. H. 2000, *ApJ*, **539**, 983
- Webb, D. F., Lepping, R. P., Burlaga, L. F., DeForest, C. E., Larson, D. E., Martin, S. F., Plunkett, S. P., & Rust, D. M. 2000, *J. Geophys. Res.*, **105**, 27251
- Williams, D. R., Török, T., Démoulin, P., van Driel-Gesztelyi, L., & Kliem, B. 2005, *ApJ*, **628**, L163
- Wu, S. T., et al. 1997, *Sol. Phys.*, **175**, 719
- Wuelser, J.-P., et al. 2004, *Proc. SPIE*, **5171**, 111
- Yang, W. H., Sturrock, P. A., & Antiochos, S. K. 1986, *ApJ*, **309**, 383
- Zhukov, A. N., & Auchère, F. 2004, *A&A*, **427**, 705